Journal of Materials Chemistry A

ROYAL SOCIETY OF CHEMISTRY

PAPER

View Article Online
View Journal | View Issue

Cite this: J. Mater. Chem. A, 2023, 11, 23001

Biomimetic integrated gas diffusion layer inspired by alveoli for enhanced air-breathing fuel cell performance and stability†

Zhi Chai,‡[ab] Fandi Ning,‡[b] Qinglin Wen,[ab] Pei Liu,[b] Can He,[ab] Wei Li,[ab] Xiong Dan,[ab] Pengpeng Xu,[b] Yiyang Liu,[b] Yali Li[ab] and Xiaochun Zhou *[abc]

Air-breathing proton exchange membrane fuel cells (air-breathing PEMFCs) have the advantages of portability, simple structure, environmental friendliness and no noise. However, due to their open cathode structure and operation environment, including gas diffusion, water and thermal management, PEMFCs are difficult to manage and largely influence the fuel cell performance and durability. In this study, inspired by alveoli, a biomimetic integrated gas diffusion layer (GDL) is designed to effectively improve the operation environment of the air-breathing PEMFC. The fuel cell using the biomimetic integrated GDL shows higher performance and more stability than a traditional fuel cell under various temperatures and wind speeds. The air-breathing PEMFC with biomimetic integrated GDL showed high performance with a peak power density of 148.5 mW cm^{-2}, which is superior to the traditional air-breathing PEMFC's density of 109.8 mW cm^{-2}. Additionally, at the cathode wind speed of 4 m s^{-1}, the fuel cell performance using the biomimetic integrated GDL only decreases by 2.38% after discharge at 150 mA cm^{-2} for 100 h, while that of the traditional fuel cell declines by 64.5% in 10 minutes. Moreover, the fuel cell stack exhibits 17.5 W at 3.17 V and the performance declines by only 11.8% after discharge for 200 h under 3.5 A. The biomimetic integrated GDL offers a simple and effective approach to achieving high performance and stability for air-breathing PEMFC.

Received 4th August 2023
Accepted 4th October 2023

DOI: 10.1039/d3ta04633h

rsc.li/materials-a

1 Introduction

Proton exchange membrane fuel cells (PEMFCs) convert chemical energy into electrical energy.[1–4] They have become one of the most promising solutions for addressing current energy depletion and environmental pollution issues due to their low pollution, high energy conversion efficiency and quick start-up.[5–10] As one of the PEMFCs, air-breathing PEMFCs offer simplified design, extended lifespan, enhanced reliability and versatile applications.[11–15]

Scheme 1a depicts the structure of the air-breathing PEMFCs, which includes an anode collector plate, membrane electrode assembly (MEA) and a cathode collector plate.[16] Oxygen is passively supplied through free diffusion to the cathode of air-breathing PEMFC, and the cathode is directly exposed to the air.[17] Oxygen reacts with hydrogen inside the fuel cell to generate water, which is discharged into the air on the cathode side.[18] Due to the open cathode structure and low temperature operation, the key challenge hindering the performance and durability of air-breathing PEMFCs is the operating environment, especially gas diffusion, water and thermal management.[19–22] Proper diffusion and distribution of oxygen within the fuel cell ensure uniform reaction rates and prevent localized depletion, enhancing overall performance and durability.[23] Excessive water accumulation impedes GDL and causes flooding, leading to reduced gas supply.[24,25] Conversely, insufficient water results in membrane dehydration and performance degradation.[26,27] In summary, gas diffusion and water and thermal management are crucial factors influencing the performance and stability of air-breathing PEMFCs.

In the past decades, researchers have made efforts to improve gas diffusion and water management in PEMFCs, particularly focusing on the GDL. There are two main approaches concerning GDL improvement. The first category is changing the wettability of the GDL to enhance its water management and gas diffusion;[28,29] this includes treating GDLs with different content PTFE or using Janus GDLs with one side hydrophilic and the other side hydrophobic.[30,31] The second category is improving the GDL structure,[32] including pore size,[33] pore shape and graded pore structure to enhance gas

[a]School of Nano Technology and Nano Bionics, University of Science and Technology of China, Hefei 230026, China. E-mail: xczhou2013@sinano.ac.cn

[b]Suzhou Institute of Nano-Tech and Nano-Bionics, Chinese Academy of Sciences (CAS), Suzhou 215123, China

[c]Key Laboratory of Precision and Intelligent Chemistry, University of Science and Technology of China, Hefei, Anhui 230026, China

† Electronic supplementary information (ESI) available. See DOI: https://doi.org/10.1039/d3ta04633h

‡ Co-first authors.

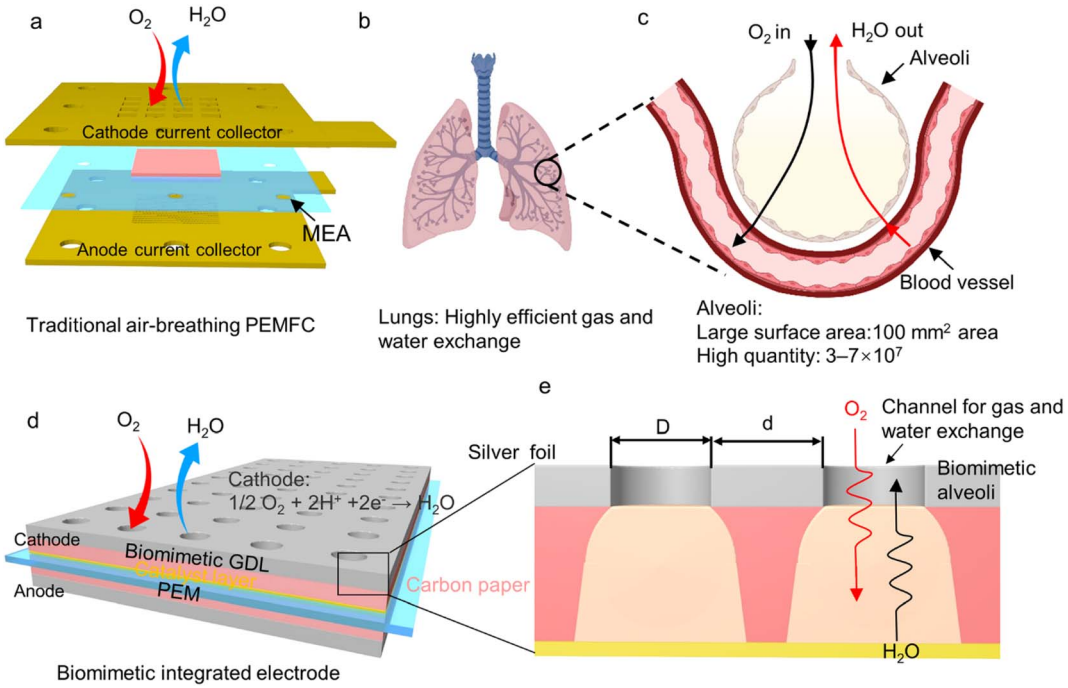

Scheme 1 Scheme of traditional air-breathing PEMFC and biomimetic integrated electrode. (a) Scheme of traditional air-breathing PEMFC. (b) Diagram of lungs. (c) Scheme of air exchange between alveoli and blood vessels. (d) Scheme of biomimetic integrated electrode. (e) Scheme of biomimetic integrated GDL. (b) and (c) are created in https://BioRender.com.

permeability.[34–36] Additionally, another solution is designing and optimizing the structure of the cathode current collector plate.[37] For example, improvements in thermal conductivity and hydrophilicity,[38,39] as well as geometric parameters of the channels, including length,[40,41] width,[42,43] height[44,45] and rib-channel ratio.[46,47]

While the solutions mentioned above have effectively improved the gas diffusion and water management capability of PEMFCs, there are three drawbacks in the current research. Firstly, most of these solutions are relatively complex to operate and difficult to control. Secondly, the regulatory intensity for water management and gas diffusion capacity in fuel cells is insufficient. Lastly, the above two methods are both separate from the study of GDL or current collector plate, and the research works should be more integrated. In conclusion, while the current research has made significant strides in enhancing gas diffusion and water management in PEMFCs, addressing the mentioned drawbacks will be critical to further advancing fuel cell technology and maximizing its potential in various applications.

As shown in Scheme 1b, the human lung is a vital organ with remarkable functions, including rapid gas exchange with the external environment, as well as regulating internal humidity and temperature. The lung's exceptional abilities offer valuable insights and potential solutions for addressing the main challenges in air-breathing PEMFCs. These functions of the lung are mainly determined by its specific structure, as illustrated in Scheme 1c. The lung is made up of numerous alveoli, with an astounding number ranging from 3 to 7 × 10^7, each alveoli providing a vast surface area of approximately 100 mm^2.[48,49] These structures work together to enable efficient gas exchange and regulate internal temperature and humidity in the lungs.[50,51] The lessons learned from the lung's natural design hold significant promise in advancing the capabilities of PEMFC technology.

Inspired by the structure of alveoli, a biomimetic integrated GDL was carefully designed (Scheme 1e). Thanks to its biomimetic alveoli structure, it improves the issues of gas diffusion and water management in air-breathing PEMFC, thereby significantly enhancing performance and durability. The biomimetic integrated GDL is composed of a perforated silver foil (depicted as the grey part in Scheme 1d and e) and carbon paper (illustrated as the pink part in Scheme 1d and e). Through meticulous design and optimization of the geometric parameters of the perforated silver foil pores, outstanding gas diffusion and water management capabilities have been achieved. As a result, the air-breathing PEMFC utilizing the biomimetic integrated GDL exhibits impressive performance, reaching a power density of 148.5 mW cm^{-2}, surpassing that of the traditional air-breathing PEMFC, which only achieves 109.8 mW cm^{-2}. Furthermore, the biomimetic integrated GDL demonstrates remarkable superiority over the traditional air-breathing PEMFC, particularly in challenging conditions like cathode high temperatures and high wind speeds. Moreover, the fuel cell using the biomimetic integrated GDL showcases superior durability compared to a traditional fuel cell. Additionally, the fuel cell stack delivers 17.5 W at 3.17 V and experiences a mere 11.8% decline after 200 hours of discharge under 3.5 A. These results highlight the efficacy of the biomimetic integrated GDL in significantly enhancing the performance and durability of

air-breathing PEMFC. Therefore, the biomimetic integrated GDL offers a simple and effective method to improve the performance and durability of air-breathing PEMFC.

2 Results and discussion

2.1 Preparation and high performance of fuel cell using biomimetic integrated GDL

Here, we propose a simple and scalable method for preparing a biomimetic integrated GDL for air-breathing PEMFC. The preparation process of the biomimetic integrated GDL involves the following two steps. Firstly, as illustrated in Fig. 1a, a high conductivity and cheap silver foil with through-pore arrays is fabricated by laser marking. Benefiting from the high conductivity of the silver foil, the silver foil serves as an excellent current collector to collect current. Simultaneously, the through-pore arrays provide channels for rapid gas diffusion and water management, resembling the function of alveoli in the lung. To achieve optimal performance, the diameter and spacing of the pore array require meticulous design. Fig. $1a_1$ displays the cross-section SEM image of the silver foil with the through-pore array, which has a thickness of 10 μm, and the pores are through. Moreover, we adjust the diameter and spacing of the pores by setting up the laser marking to better mimic the function of alveoli.

Secondly, to obtain the biomimetic integrated GDL, the silver foil with through-pore arrays and commercial carbon paper were combined using conductive silver pastes, as depicted in Fig. 1b. The conductive silver pastes serve as a bonding agent. Fig. $1b_1$ illustrates the cross-section SEM image of the biomimetic integrated GDL. There is no obvious gap between the perforated silver foil and the commercial carbon paper, and the two are tightly bonded.

After preparing the biomimetic integrated GDL, the corresponding biomimetic integrated electrode was fabricated as depicted in Fig. 1c. The biomimetic integrated GDL was applied to both the anode and cathode sides, serving not only as a GDL but also as a current collector. Fig. $1c_1$ displays a cross section SEM image of the biomimetic integrated electrode. The fundamental shape is still preserved during the preparation of the biomimetic integrated electrode. Subsequently, the assembly of the fuel cell was carried out. Fig. 1d displays the optical images of the biomimetic air-breathing PEMFC, while Fig. 1e shows the optical images of the traditional air-breathing PEMFC. The biomimetic air-breathing PEMFC utilizes a biomimetic integrated GDL that also functions as a current collector, resulting in a simpler structure compared to the traditional PEMFC, which requires an additional current collector, often made of porous metal or graphite plates. Benefiting the well-designed structure and the optimization of the biomimetic

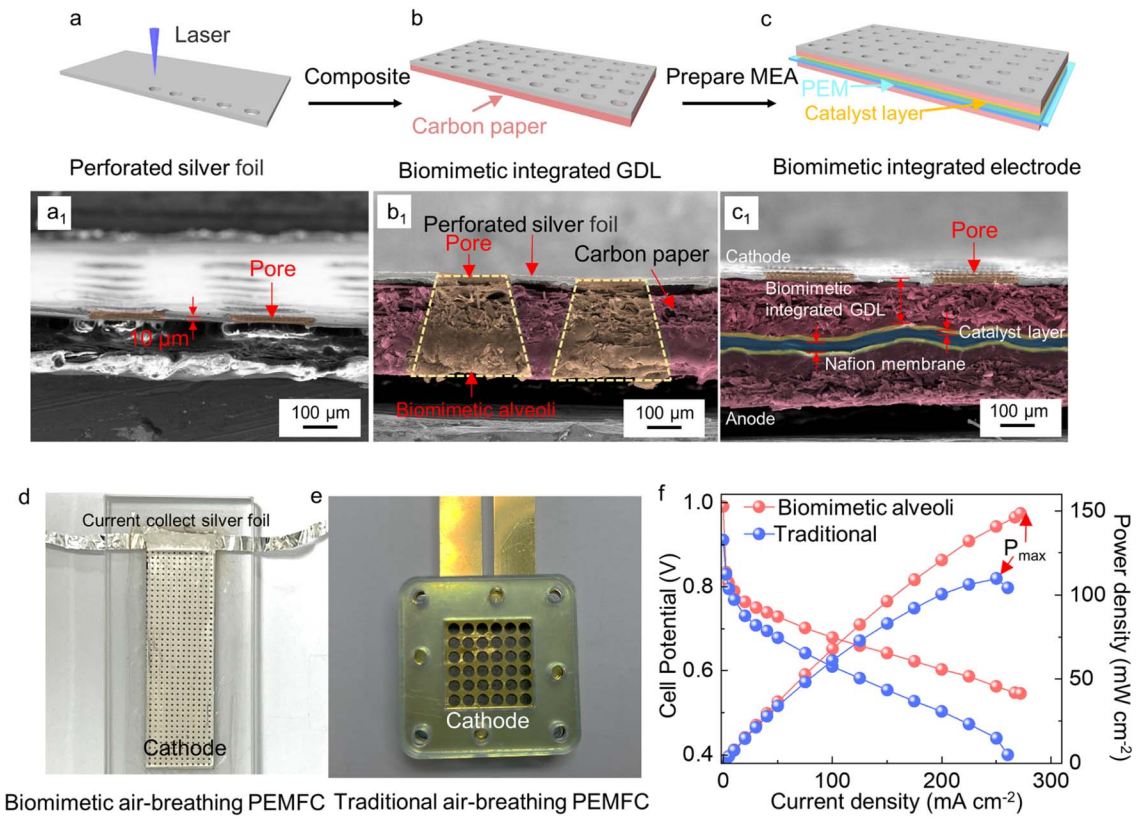

Fig. 1 Preparation and high performance of fuel cell using biomimetic integrated GDL. (a) Preparation of perforated silver foil. (b) Preparation of biomimetic integrated GDL. (c) Preparation of biomimetic integrated electrode. (d) Photograph of biomimetic air-breathing PEMFC. (e) Photograph of traditional air-breathing PEMFC. (f) The polarization curves of biomimetic PEMFC and traditional PEMFC. The active area of fuel cell is 2.5 cm × 8 cm, *i.e.*, 20 cm^2. (a_1–c_1) Cross section SEM image of (a–c). Refer to ESI 4† for the original version of SEM image.

integrated GDL, the biomimetic air-breathing PEMFC achieves higher performance compared to the traditional. Fig. 1f illustrates the polarization curves of the biomimetic air-breathing PEMFC and the traditional air-breathing PEMFC. The peak power density (P_{max}) of the biomimetic air-breathing PEMFC is 148.5 mW cm^{-2}, which is significantly superior to the 109.8 mW cm^{-2} of the traditional air-breathing PEMFC.

2.2 Optimization of the alveoli size in the biomimetic GDL

The superior performance of maintaining stable internal humidity and rapid gas exchange of alveoli is closely related to the size and number of the alveoli. Fig. 2a illustrates the research conducted on the alveoli size of the biomimetic integrated GDL by adjusting the opening diameter (D) while keeping the spacing constant (d, 0.2 mm). The opening diameter varies from 0.2 to 1.1 mm. In Fig. 2b, a photograph of perforated silver foil is shown, with a pore opening diameter of 0.2 mm and a spacing of 0.2 mm. Conversely, Fig. 2c shows a photograph of perforated silver foil with a pore opening diameter of 1.1 mm and a spacing of 0.2 mm. It is evident that as the biomimetic alveoli opening diameter increases, the number of alveoli per unit area decreases gradually. The research conducted on the alveoli size plays a crucial role in understanding the optimal configuration that mimics the natural efficiency of gas diffusion and water management observed in biological alveoli.

Fig. 2d shows the polarization curves of fuel cells using the biomimetic integrated GDL with different opening diameters. The varied opening diameters ranging from 0.2 to 1.1 mm have a significant impact on the fuel cell performance. Specifically, as depicted in Fig. 2e, the P_{max} initially increases and then decreases with the increase in the opening diameter. In Fig. 2f, it is evident that as the biomimetic alveoli opening diameter increases from 0.2 mm to 0.7 mm, there is a corresponding increase in P_{max} by 37.7 mW cm^{-2}. However, when the biomimetic alveoli opening diameter is further increased from 0.7 mm to 1.1 mm, the P_{max} subsequently decreases by 17.2 mW cm^{-2}. The optimized diameter is 0.7 mm, and the P_{max} is 132.1 mW cm^{-2}

The effect of the opening diameter on fuel cell performance is explained from the following aspects. Firstly, Fig. 2f

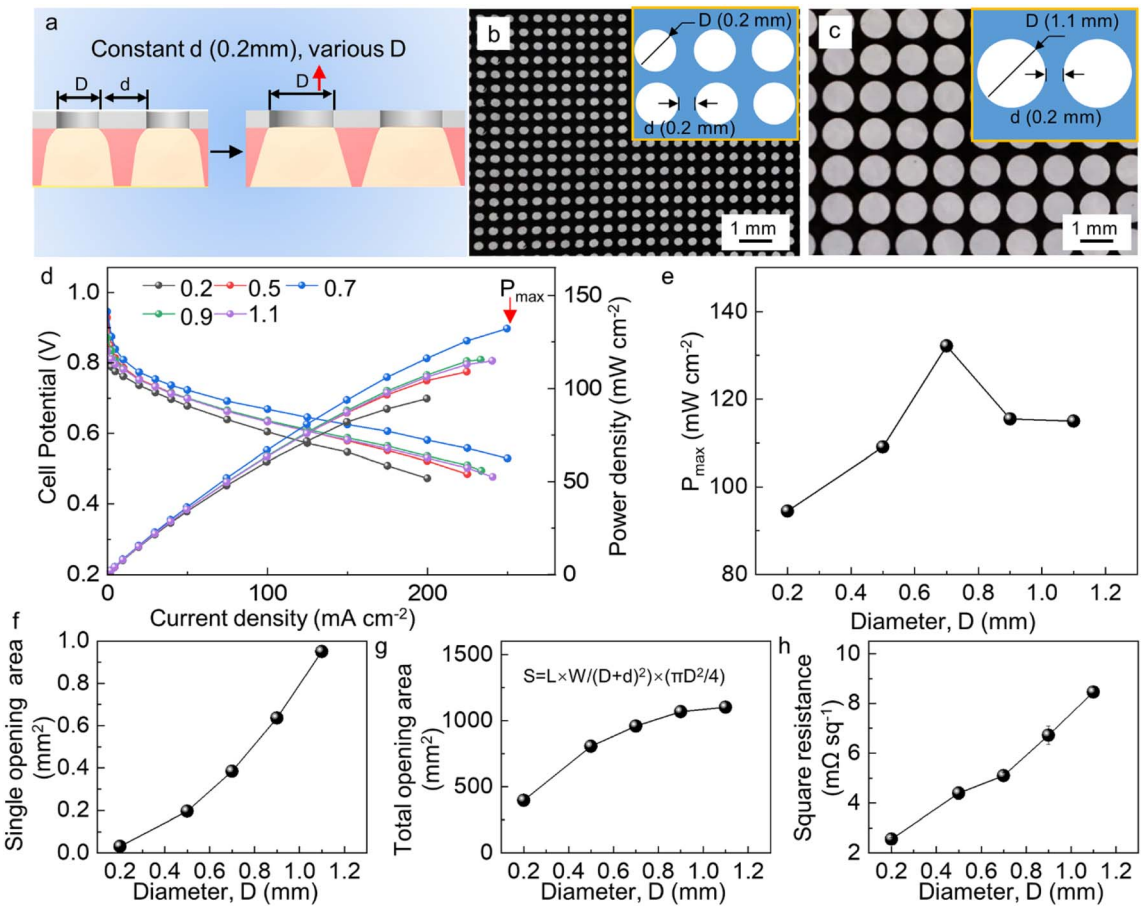

Fig. 2 Optimization of alveoli size in the biomimetic GDL. (a) Scheme of biomimetic alveoli opening diameter (D) enlarging. (b) A photograph of perforated silver foil with a pore opening diameter of 0.2 mm and a spacing of 0.2 mm. (c) A photograph of perforated silver foil with a pore opening diameter of 1.1 mm and a spacing of 0.2 mm. The insert are schematic diagrams. (d) The polarization curves of fuel cells using biomimetic integrated GDL with different opening diameter. (e) The peak power density (P_{max}). (f)–(h) The relationship between the biomimetic alveoli opening diameter and single opening area, total opening area, square resistance. S represents the total opening area. S, L, and W are the total opening area, length, and width of the biomimetic integrated GDL.

illustrates the relationship between the opening diameter and the opening area. Clearly, as the opening diameter increases, the opening area also increases. Fig. 2g displays the total opening area for different opening diameters. As the diameter increases from 0.2 to 1.1 mm, the total opening area also increases, ranging from 395.6 to 1100.1 mm^2. On the one hand, the large total opening area provides more gas and water transport channels, making fuel cells less prone to flooding and offering more gas transport channels. This benefits the improvement of the fuel cell performance. On the other hand, the large total opening area provides more water transport channels, and the Nafion membrane will easily dry out. This, in turn, increases the inner resistance of the fuel cell, resulting in decreased fuel cell performance. Second, Fig. 2h shows that the square resistance of the biomimetic integrated GDL always remains in the range of 2.56 to 8.46 mΩ sq^{-1}, which does not significantly impact the current collection.

Thus, the diameter influences gas diffusion and water management. On the one hand, a larger diameter proves beneficial for improving gas diffusion and provides more water transport channels, making fuel cells less prone to flooding and subsequently enhancing fuel cell performance. On the other hand, it also negatively impacts water retention, leading to the Nafion membrane drying out and further impairing fuel cell performance. Therefore, there exists an optimal diameter of 0.7 mm and an optimal fuel cell performance of 132.1 mW cm^{-2}. This finding highlights the importance of carefully balancing the biomimetic alveoli opening diameter to achieve optimal gas diffusion and water management.

2.3 Optimization of alveoli number in the biomimetic GDL

The number of alveoli is another important parameter that plays a crucial role in achieving the desired lung-like function in the biomimetic integrated GDL. Therefore, the alveoli number of the biomimetic integrated GDL was optimized by adjusting the opening spacing. Based on the results above, the diameter was fixed at 0.7 mm, while the spacing ranged from 0.2 to 1.9 mm. As depicted in Fig. 3a, it is evident that the alveoli number decreases notably with the increase in the opening spacing while the opening area remains constant. In Fig. 3b, a photograph of the perforated silver foil with pore opening diameter of

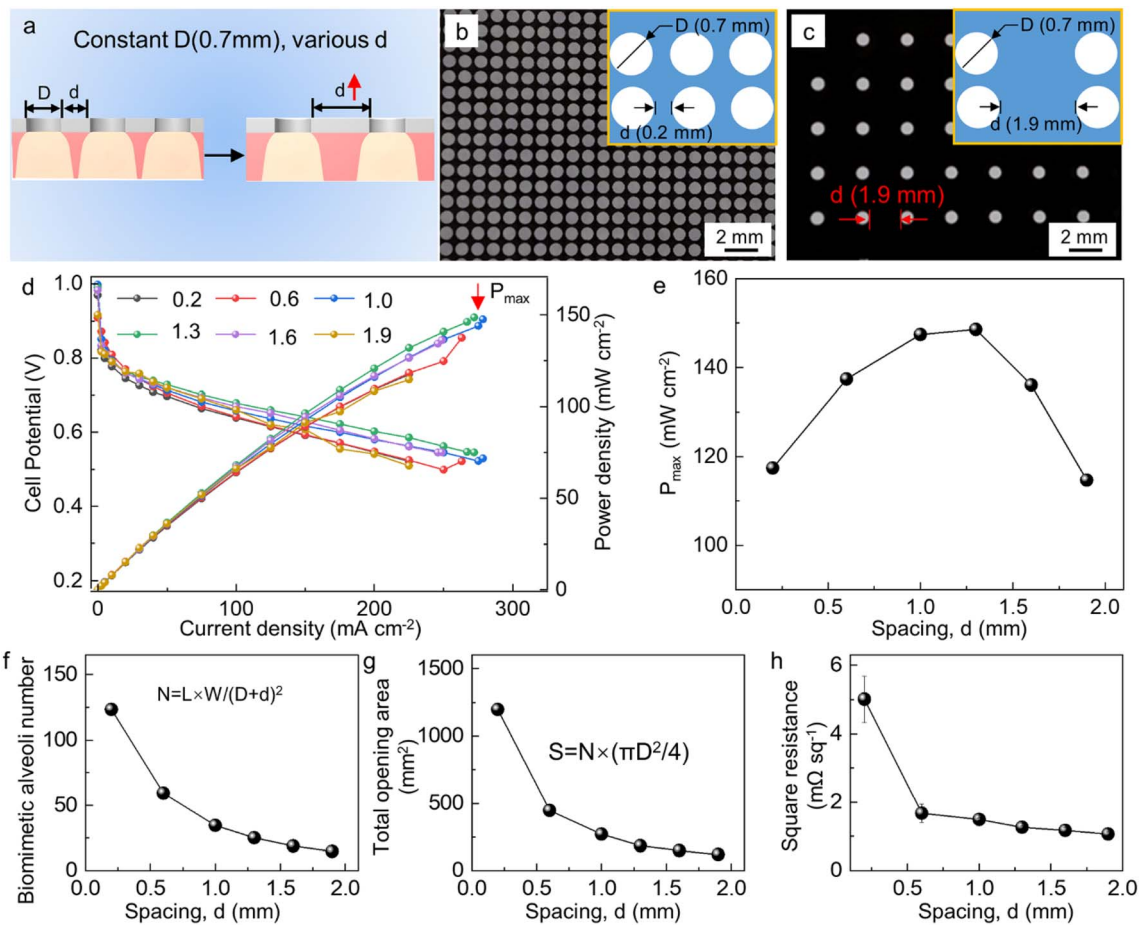

Fig. 3 Optimization of alveoli number in the biomimetic GDL. (a) Scheme of biomimetic alveoli opening spacing (*d*) enlarging. (b) A photograph of perforated silver foil with a pore opening diameter of 0.7 mm and a spacing of 0.2 mm. (c) A photograph of perforated silver foil with a pore opening diameter of 0.7 mm and a spacing of 1.9 mm. The insert are schematic diagrams. (d) The polarization curves of fuel cells using biomimetic integrated GDL with different opening spacing. (e) The peak power density (P_{max}). (f–h) The relationship between the biomimetic alveoli opening spacing and biomimetic alveoli number, total opening area and square resistance. *N* is the biomimetic alveoli number.

0.7 mm and spacing of 0.2 mm is presented, while Fig. 3c displays a photograph of the perforated silver foil with pore opening diameter of 0.2 mm and spacing of 1.9 mm. It can be observed that as the biomimetic alveoli opening spacing increases, the number of alveoli gradually decreases. Consequently, this reduction results in fewer channels for gas and water transport per unit area. The optimization of alveoli number is critical in ensuring efficient gas and water management, which directly influences the overall performance of the fuel cell.

Fig. 3d presents the polarization curves of the fuel cells using the biomimetic integrated GDL with different opening spacing. The fuel cell performance is influenced by the variation in opening spacing, showing a similar trend of initially increasing and then decreasing as the biomimetic alveoli opening spacing increases. In detail, when the biomimetic alveoli opening spacing increases from 0.2 mm to 1.3 mm, the P_{max} increases by 31.2 mW cm^{-2} (Fig. 3f). However, when the biomimetic alveoli opening spacing further increases from 1.3 mm to 1.9 mm, the P_{max} subsequently decreases by 33.8 mW cm^{-2}. Therefore, the optimized spacing is determined to be 1.3 mm and an optimal fuel cell performance of 148.5 mW cm^{-2}, significantly higher than that of traditional air-breathing PEMFCs with a P_{max} of 109.8 mW cm^{-2}.

Fig. 3f demonstrates that as the biomimetic alveoli opening spacing gradually increases, the total number of biomimetic alveoli decreases. For instance, when the spacing increases from 0.2 to 1.9 mm, the biomimetic alveoli number decreases from 123 to 16 per square centimeter. In Fig. 3g, it is evident that as the biomimetic alveoli opening spacing gradually increases, the total opening area also decreases. When the spacing increases from 0.2 to 1.9 mm, the total biomimetic alveoli opening area decreases from 1198 to 119 mm^2. The impact of the biomimetic alveoli opening spacing on fuel cell performance is understood from these observations. On the one hand, a small total opening area offers fewer gas diffusion channels, which may not be conducive to improving fuel cell performance. On the other hand, a small total opening area also provides fewer water transport channels, which is beneficial for increasing the water content of the Nafion membrane. This, in turn, reduces the proton resistance and enhances fuel cell performance. However, if the total opening area is too small, it will lead to fuel cell flooding and significantly reduced gas diffusion, consequently diminishing its overall performance. Fig. 3h shows that the square resistance of the biomimetic integrated GDL always remains between 5.01 and 1.07 mΩ sq^{-1}, which has no impact on the collection of current.

The spacing within the biomimetic integrated GDL indeed plays a crucial role in gas diffusion and water management. A larger opening spacing is advantageous for retaining water in the Nafion membrane, leading to a further increase in fuel cell performance. However, excessively large opening spacing will lead to delayed water discharge or even flooding, which is not conducive to efficient gas diffusion and can impair fuel cell performance. Consequently, an optimal diameter of 1.3 mm and an optimal fuel cell performance of 148.5 mW cm^{-2} have been identified. This finding underscores the significance of carefully selecting both the alveoli diameter and spacing to strike an ideal balance between gas diffusion, water management, and overall fuel cell performance.

2.4 Resist multiple wind speeds and maintain stable water management

Traditional air-breathing PEMFCs, especially the fuel cell stack, typically require an excess air supply. This excess air is essential for dissipating heat to prevent the stack from overheating and to ensure an ample oxygen supply for the electrochemical reactions. Additionally, as the air metering ratio, *i.e.*, wind speed, increases, the water generated on the cathode side is quickly carried away from the fuel cell, converting into steam in the air (Fig. 4a). However, excessive evaporation of water can lead to Nafion membrane dehydration, resulting in an increase in the internal resistance of the fuel cell and further diminishing the performance and stability of the fuel cell. It is crucial to carefully manage the air supply to maintain optimal operating conditions and prevent undesirable effects on fuel cell performance caused by excessive water evaporation.

The structure of the biomimetic integrated GDL effectively maintains the internal environment, particularly the humidity, within the fuel cell. As a result, the fuel cell using the biomimetic integrated GDL demonstrates excellent resistance to multiple wind speeds. Fig. 4a shows the test device and a fan is placed in front of the fuel cell. The impact of different wind speeds on fuel cell performance is simulated by adjusting the fan wind speed. In Fig. 4b, the peak power density (P_{max}) of the fuel cell is presented with different alveoli numbers (*i.e.*, the opening spacing) at various wind speeds. Specific polarization curves can be found in ESI 5.† Overall, it can be observed that increasing wind speed leads to a varying degree of decrease in fuel cell performance when using the biomimetic integrated GDL with different spacings and the traditional air-breathing PEMFC.

In order to see the impact of wind speed more clearly on the P_{max} of fuel cells, we normalized the P_{max} of fuel cells under different wind speeds. As shown in Fig. 4c, for biomimetic integrated electrodes with a spacing of 1.0, 1.3, and 1.6 mm, the corresponding P_{max} amplitudes are 0.033, 0.019, and 0.010, respectively. It is clearly seen that with larger spacing, the amplitude of P_{max} attenuation gradually decreases with the increase in wind speed. This is mainly because the spacing determines the density of the biomimetic alveoli, and a larger spacing results in a lower biomimetic alveoli density. At a lower biomimetic alveoli density, *i.e.*, spacing of 1.6 mm, even with an increase in wind speed, water evaporation becomes limited. If water cannot be discharged promptly, it may cause flooding and further lead to the degradation of fuel cell performance. Conversely, at a higher biomimetic alveoli density, *i.e.*, spacing of 1.0 mm, faster wind speed promotes the rapid evaporation of water, leading to a dried Nafion membrane and a decline in fuel cell performance. Therefore, there exists a reasonable biomimetic alveoli density, and when the biomimetic alveoli opening spacing is 1.3 mm, the water content inside the fuel cell is within a reasonable range, further ensuring that the fuel cell

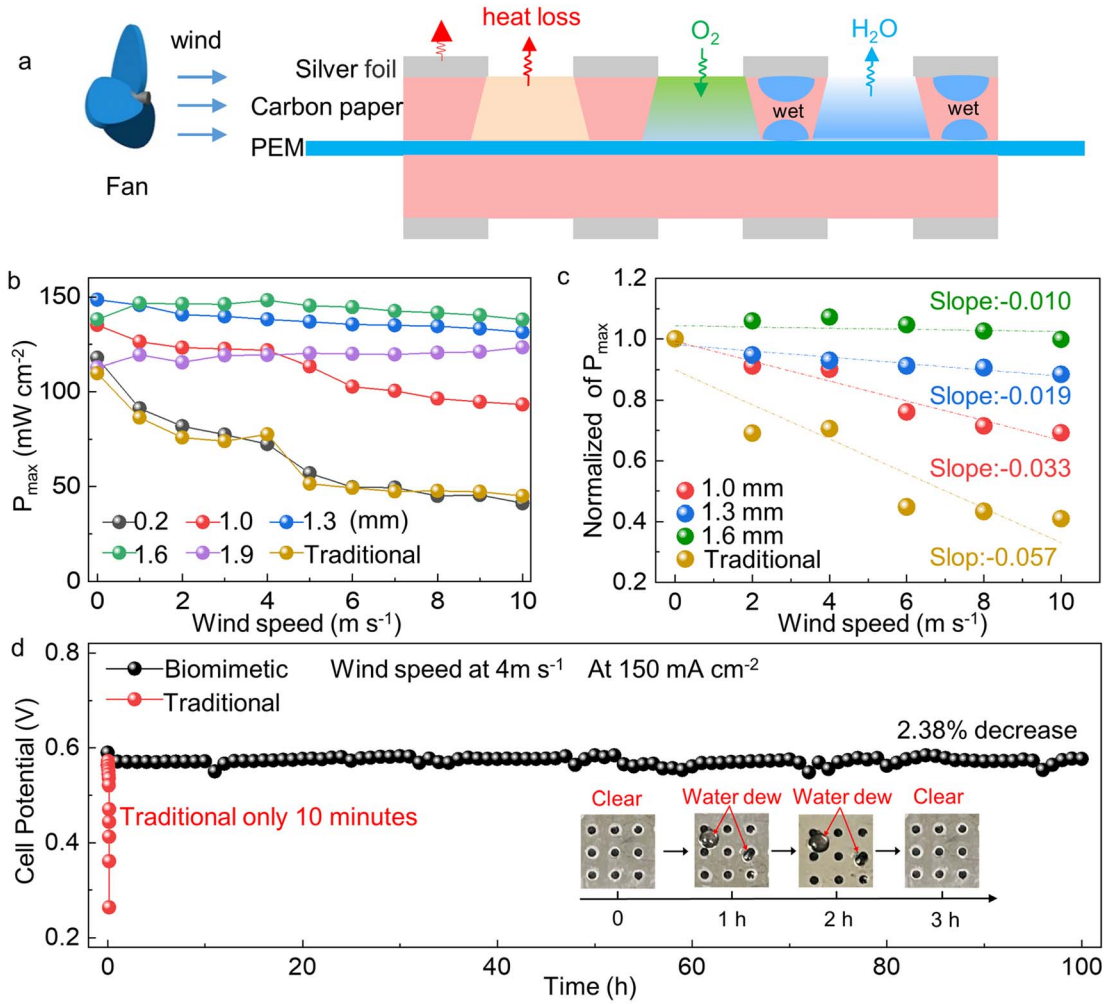

Fig. 4 The fuel cell resisting multiple wind speeds and maintaining stable water management. (a) Schematic diagram of testing device for fuel cell resistance to different wind speeds. (b) Peak power density (P_{max}) of the fuel cells at different wind speeds. (c) Normalization of peak power density (P_{max}) of fuel cells under different wind speeds. (d) Constant current discharge at 150 mA cm^{-2} of biomimetic air-breathing PEMFC versus traditional air-breathing PEMFC, and the wind speed is 4 m s^{-1}.

always has stable performance under varying wind speeds. The P_{max} attenuation of the fuel cells prepared with biomimetic integrated GDLs in the presence of wind speed has consistently been much lower than that of the traditional fuel cell (0.057), thereby fully demonstrating the enormous advantage of biomimetic integrated GDL in maintaining internal water management in fuel cells.

The ability of biomimetic integrated GDL to maintain internal water content in fuel cells is beneficial for improving its stability. As demonstrated in Fig. 4d, a traditional fuel cell discharges at a constant current of 150 mA cm^{-2} for 10 min, and the voltage decays from 0.56 V to 0.2 V, resulting in a significant decrease of 64.3%. The fuel cell prepared with biomimetic integrated GDL (opening spacing 1.3 mm) achieved superior stability discharge under the same current density. After 100 h, the voltage degradation of the fuel cell was only 2.38%. This impressive stability of the biomimetic air-breathing PEMFC can be attributed to its superior water retention capabilities. Fig. 4d presents the surface photograph of the biomimetic air-breathing PEMFC cathode during constant current discharge. Water dew began to appear after 1 h and disappeared after 3 h. As can be observed in Fig. 4d, during constant current operation, the fluctuation of discharge voltage is small, showcasing the exceptional capacity of biomimetic alveoli to maintain a stable water content of the fuel cell's internal environment. Consequently, the biomimetic air-breathing PEMFC achieved both superior performance and long-term stability, underscoring the significant advantages of this design in maintaining proper water management within the fuel cell.

2.5 Adaptability under different temperatures

The ability of biomimetic integrated GDL to maintain the internal environment was further demonstrated through testing at different temperatures. Excessive temperature leads to increased water evaporation, causing dehydration of the Nafion membrane and ultimately compromising fuel cell performance. Fig. S5† shows the experimental devices, with a heating platform positioned under the fuel cell cathode and

a thermocouple for measuring the temperature of the cathode. The tests were conducted to assess the biomimetic integrated GDL performance under varying temperature conditions, ensuring its capability to manage water content and prevent detrimental effects on fuel cell operation.

The temperature increase has two main effects on the fuel cell. Firstly, it leads to increased water discharge from the fuel cell. Secondly, higher temperatures favor faster chemical reactions from a chemical kinetics perspective. Fig. 5a illustrates the variation of P_{max} with increasing temperature for fuel cells with different biomimetic alveoli numbers (opening spacing), and specific polarization curves can be found in ESI 7.† It can be clearly seen that changes in temperature will have an impact on the performance of both traditional fuel cells and those using biomimetic integrated GDL. The temperature sensitivity of the fuel cell performance underscores the importance of proper water management, and the biomimetic integrated GDL ability to mitigate water loss becomes crucial in maintaining stable and efficient fuel cell operation under varying temperature conditions.

The normalization treatment of P_{max} at different temperatures in Fig. 5b provides a clearer depiction of the impact of temperature on P_{max}. When the spacing is 1.0, 1.3, and 1.6 mm, the decay rates of P_{max} are 0.012, 0.0092, and 0.0095, respectively. Overall, the larger the spacing, the smaller the attenuation amplitude of P_{max} with increasing temperature. This is mainly because the larger the spacing, the lower the density of the biomimetic alveoli, and the fewer channels for water to be discharged from the fuel cell, leaving more water inside the fuel cell. As a result, at high temperatures, fuel cells with larger biomimetic alveoli opening spacing exhibit better performance. Furthermore, with the increase in temperature, the P_{max} attenuation rate of traditional fuel cells is 0.017, which is much faster than that of fuel cells with biomimetic integrated GDLs. This demonstrates that the biomimetic integrated GDL effectively resists the evaporation and loss of water at different temperatures, continuously maintaining the water content inside the fuel cell within a reasonable range and thus sustaining the overall fuel cell performance. The superior water retention capability of the biomimetic GDL contributes significantly to its ability to maintain stable and efficient fuel cell operation under varying temperature conditions.

2.6 High performance and durability of the fuel cell stack using biomimetic integrated GDL

The advantages of the biomimetic integrated GDL are further demonstrated in high performance and durable fuel cell stacks. Fig. 6a illustrates a fuel cell stack consisting of six individual fuel cells (the fuel cell stack size and mass parameters can be found in ESI 11†). The adjacent anode sides of the fuel cells are sealed in a face-to-face configuration and secured onto a hollow plastic support plate. The plastic support plate and columns stabilize the stack structure. All fuel cells in the stack are connected in series, and the adjacent cells are connected by silver plates to link the cathode and anode. The polarization curves of six individual fuel cell is depicted in Fig. S7.†

Fig. 6b shows an optical image of the fuel cell stack consisting of six series-connected fuel cells. Fig. 6c represents the polarization curve of the stack. The fuel cell stack achieves a power output of 17.5 W (5.5 A, 3.17 V). Furthermore, the fuel cell stack also exhibits outstanding durability. As shown in Fig. 6d, the fuel cell stack only experiences an 11.8% decline in performance after discharging at 3.5 A for 200 h. The high durability of the fuel cell stack is benefited by the superior ability of the biomimetic integrated GDL to maintain the internal environment of the fuel cell. Throughout the discharge process (Fig. S8†), the temperature of the fuel cell stack remains stable, around 50 °C, with a slight temperature distribution imbalance. Localized high temperatures can accelerate processes such as carbon corrosion, Pt dissolution, and Pt/C oxidation.[52–54] Non-uniform temperature distribution can also lead to localized flooding and dehydration, which can accelerate the aging of the proton exchange membrane and even result in the detachment of the proton exchange membrane from the GDL.[55–57] These factors have a significant impact on the durability of the stack. Therefore, in comparison to a single fuel cell, the stack experiences a much higher decay rate.

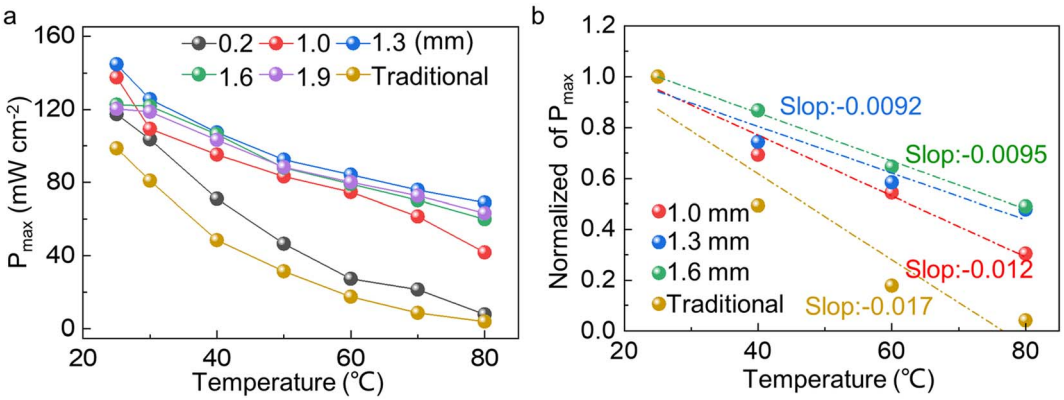

Fig. 5 Biomimetic integrated GDL maintains stable internal humidity in air-breathing PEMFC under different temperature. (a) The effect of temperature on the P_{max} of different number of biomimetic alveoli. (b) The normalization of P_{max} changes the number of biomimetic alveoli at each temperature.

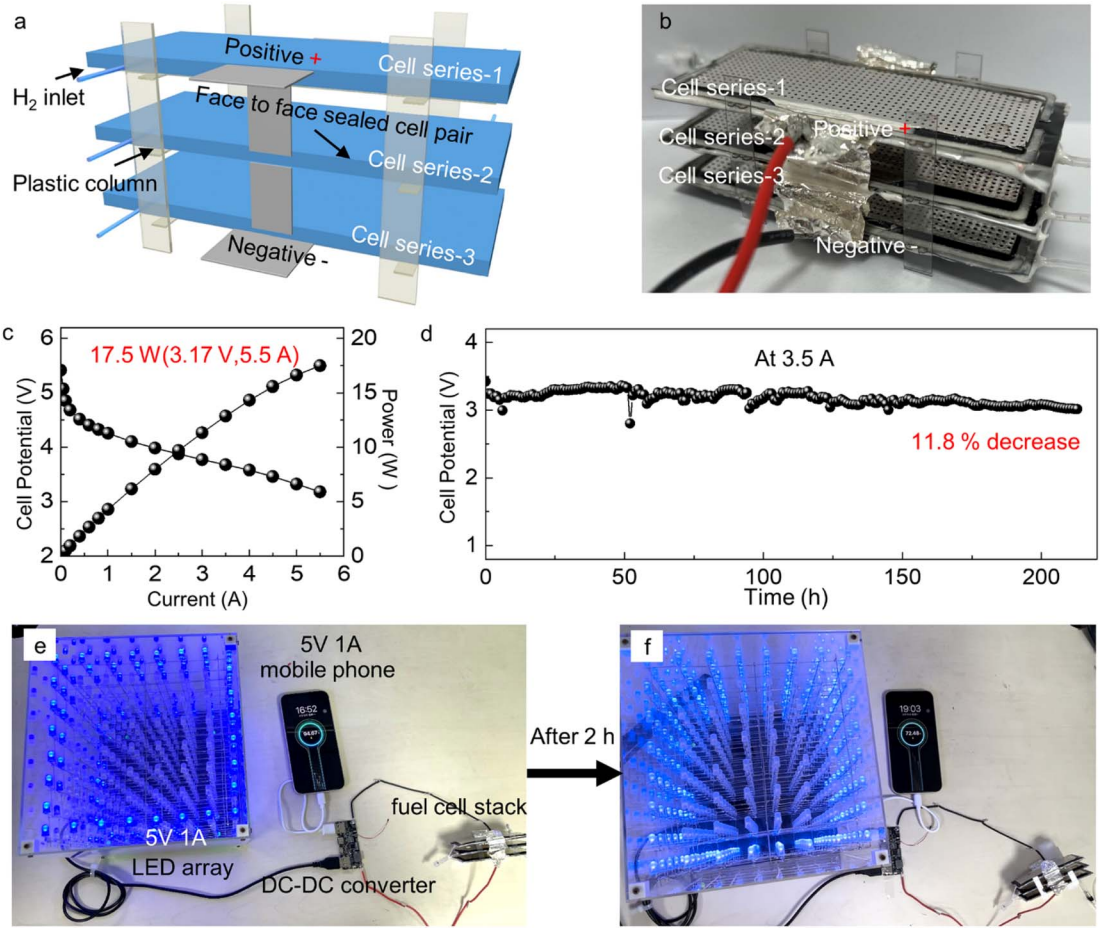

Fig. 6 High performance and durability of the fuel cell stack using biomimetic integrated GDL. (a) Scheme of fuel cell stack with six single fuel cells in series. The active area of a single fuel cell is 2.5 cm × 8 cm, *i.e.*, 20 cm^2. (b) Optical photo of air-breathing fuel cell stack with six single fuel cells in series. (c) Polarization curve of fuel cell stack. (d) Constant current discharge (3.5 A for 200 h) of fuel cell stack. (e and f) Optical photo of fuel cell stack powers for one mobile phone and one LED array for 2 h.

To further demonstrate the practical application value of the fuel cell stack, it was employed to power a mobile phone and an LED array for 2 h (Fig. 6e and f). These results highlight the potential of the biomimetic integrated GDL in enabling high-performance and durable fuel cell stacks. These results highlight the significant potential of the biomimetic integrated GDL in enabling high-performance and durable fuel cell stacks, making it a promising technology for various practical applications.

3 Conclusions

Inspired by the alveoli, a biomimetic integrated GDL with a simple fabrication method and few steps was designed to improve the performance and durability of air-breathing PEMFC. The biomimetic integrated GDL includes silver foil with a through-pore array and commercial carbon paper. The adjustment of the geometrical parameters (spacing, diameter) enhances gas diffusion and water management. The fuel cell using the biomimetic integrated GDL shows a high peak power density of 148.5 mW cm^{-2}, far superior to the traditional air-breathing PEMFC of 109.8 mW cm^{-2}. Moreover, the fuel cell using the biomimetic integrated GDL exhibits exceptional durability, with only a 2.83% decline in performance after continuous discharge at 150 mA cm^{-2} for 200 h. Benefiting from the biomimetic structure of the biomimetic integrated GDL, the fuel cell resists different wind speeds and temperatures and always maintains high performance and durability. In addition, the fuel cell stack assembled using the biomimetic integrated GDL exhibits a high current of 5.5 A and high power of 17.5 W at 3.17 V. Furthermore, the fuel cell stack is practical as it simultaneously charges mobile phones and power electronic devices for more than 2 h. This versatility and reliability make the biomimetic integrated GDL suitable for deployment in demanding environments, such as drone and military equipment fuel cells. Overall, the biomimetic integrated GDL technology holds great promise for enhancing fuel cell performance and advancing the development of efficient and robust energy solutions.

Author contributions

Zhi Chai and Fandi Ning contributed equally to this work. Zhi Chai and Fandi Ning designed the experiments, analyzed the data, and drafted the manuscript. Qinglin Wen and Pei Liu: suggested the experiments and data analysis. Can He, Wei Li

and Xiong Dan: provided some help in SEM and methods of experiments details. Pengpeng Xu, Yiyang Liu and Yali Li provided suggestions for figures and writing the analysis. Xiaochun Zhou: supervision, suggested the experiment and data analysis, revised this manuscript.

Conflicts of interest

There are no conflicts to declare.

Acknowledgements

The authors are grateful for financial support granted by the National Key R&D Program of China from the Ministry of Science and Technology of China (no. 2020YFB1505700), Science and Technology Program of Suzhou (No. ST202214, SYC2022100). The authors are grateful for the technical support for Nano-X from Suzhou Institute of Nano-Tech and Nano-Bionics, Chinese Academy of Sciences (SINANO).

References

1 S. Tanaka and T. Shudo, *J. Power Sources*, 2014, **248**, 524–532.
2 C. Bao, M. Ouyang and B. Yi, *Int. J. Hydrogen Energy*, 2006, **31**, 1879–1896.
3 B. C. H. Steele and A. Heinzel, *Nature*, 2001, **414**, 345–352.
4 A. S. Arico, P. Bruce, B. Scrosati, J. M. Tarascon and W. Van Schalkwijk, *Nat. Mater.*, 2005, **4**, 366–377.
5 J. Jewell, D. McCollum, J. Emmerling, C. Bertram, D. Gernaat, V. Krey, L. Paroussos, L. Berger, K. Fragkiadakis, I. Keppo, N. Saadi, M. Tavoni, D. van Vuuren, V. Vinichenko and K. Riahi, *Nature*, 2018, **554**, 229–233.
6 I. Staffell, D. Scamman, A. Velazquez Abad, P. Balcombe, P. E. Dodds, P. Ekins, N. Shah and K. R. Ward, *Energy Environ. Sci.*, 2019, **12**, 463–491.
7 U. Eberle, B. Müller and R. von Helmolt, *Energy Environ. Sci.*, 2012, **5**, 8780–8798.
8 E. S. Hanley, J. P. Deane and B. P. Ó. Gallachóir, *Renewable Sustainable Energy Rev.*, 2018, **82**, 3027–3045.
9 A. Sgobbi, W. Nijs, R. De Miglio, A. Chiodi, M. Gargiulo and C. Thiel, *Int. J. Hydrogen Energy*, 2016, **41**, 19–35.
10 C. Pak, S. W. Lee, C. Baik, B. H. Lee, D. J. You and E. You, *Chin. Chem. Lett.*, 2019, **30**, 1186–1189.
11 T. V. Nguyen, *Electrochem. Soc.*, 2006, **3**, 1171–1180.
12 P. L. Hentall, J. B. Lakeman, G. O. Mepsted, P. L. Adcock and J. M. Moore, *J. Power Sources*, 1999, **80**, 235–241.
13 K. Jiao and B. Zhou, *J. Power Sources*, 2007, **169**, 296–314.
14 S. U. Jeong, E. A. Cho, H. J. Kim, T. H. Lim, I. H. Oh and S. H. Kim, *J. Power Sources*, 2006, **158**, 348–353.
15 S. Neatu, F. Neatu, I. M. Chirica, I. Borbath, E. Talas, A. Tompos, S. Somacescu, P. Osiceanu, M. A. Folgado, A. M. Chaparro and M. Florea, *J. Mater. Chem. A*, 2021, **9**, 17065–17128.
16 F. D. Ning, Y. B. Shen, C. Bai, J. Wei, G. B. Lu, Y. Cui and X. C. Zhou, *Chin. Chem. Lett.*, 2019, **30**, 1282–1288.
17 N. Bussayajarn, H. Ming, K. K. Hoong, W. Y. M. Stephen and C. S. Hwa, *Int. J. Hydrogen Energy*, 2009, **34**, 7761–7767.
18 O. Z. Sharaf and M. F. Orhan, *Renewable Sustainable Energy Rev.*, 2014, **32**, 810–853.
19 P. Manoj Kumar and V. Parthasarathy, *Energy*, 2013, **51**, 457–461.
20 M. Higuita Cano, S. Kelouwani, K. Agbossou and Y. Dubé, *J. Power Sources*, 2014, **246**, 650–658.
21 A. Mahdavi, A. A. Ranjbar, M. Gorji and M. Rahimi-Esbo, *Appl. Energy*, 2018, **228**, 656–666.
22 Z. Xu, D. Qiu, P. Yi, L. Peng and X. Lai, *Prog. Nat. Sci.: Mater. Int.*, 2020, **30**, 815–824.
23 Y. Wang, K. S. Chen, J. Mishler, S. C. Cho and X. C. Adroher, *Appl. Energy*, 2011, **88**, 981–1007.
24 H. Li, Y. Tang, Z. Wang, Z. Shi, S. Wu, D. Song, J. Zhang, K. Fatih, J. Zhang, H. Wang, Z. Liu, R. Abouatallah and A. Mazza, *J. Power Sources*, 2008, **178**, 103–117.
25 M. Ji and Z. Wei, *Energies*, 2009, **2**, 1057–1106.
26 A. T. Howe and M. G. Shilton, *J. Solid State Chem.*, 1979, **28**, 345–361.
27 K.-D. Kreuer, A. Rabenau and W. Weppner, *Angew Chem. Int. Ed. Engl.*, 1982, **21**, 208–209.
28 T. Kitahara, H. Nakajima, M. Inamoto and K. Shinto, *J. Power Sources*, 2014, **248**, 1256–1263.
29 T. Kitahara, H. Nakajima, M. Inamoto and M. Morishita, *J. Power Sources*, 2013, **234**, 129–138.
30 Q. Wen, S. Pan, Y. Li, C. Bai, M. Shen, H. Jin, F. Ning, X. Fu and X. Zhou, *ACS Energy Lett.*, 2022, **7**, 3900–3909.
31 P. K. Sinha, P. P. Mukherjee and C.-Y. Wang, *J. Mater. Chem.*, 2007, **17**, 3089–3103.
32 C. Csoklich, T. J. Schmidt and F. N. Büchi, *Energy Environ. Sci.*, 2022, **15**, 1293–1306.
33 P. Ferreira-Aparicio and A. M. Chaparro, *Int. J. Hydrogen Energy*, 2014, **39**, 3997–4004.
34 J. H. Chun, D. H. Jo, S. G. Kim, S. H. Park, C. H. Lee, E. S. Lee, J.-Y. Jyoung and S. H. Kim, *Renewable Energy*, 2013, **58**, 28–33.
35 H. Tang, S. Wang, M. Pan and R. Yuan, *J. Power Sources*, 2007, **166**, 41–46.
36 I. Bae, B. Kim, D.-Y. Kim, H. Kim and K.-H. Oh, *Renewable Energy*, 2020, **146**, 960–967.
37 S. Xing, C. Zhao, J. Zou, S. Zaman, Y. Yu, H. Gong, Y. Wang, M. Chen, M. Wang, M. Lin and H. Wang, *Renewable Sustainable Energy Rev.*, 2022, **165**, 112558.
38 J. Wu, S. Galli, I. Lagana, A. Pozio, G. Monteleone, X. Z. Yuan, J. Martin and H. Wang, *J. Power Sources*, 2009, **188**, 199–204.
39 I. Tolj, E. Penga, D. Vukievi and F. Barbir, *Appl. Energy*, 2019, **257**, 114038.
40 A. P. Sasmito, E. Birgersson, K. W. Lum and A. S. Mujumdar, *Renewable Energy*, 2012, **37**, 325–332.
41 C. Zhao, S. Xing, W. Liu, M. Chen and H. Wang, *Renewable Energy*, 2021, **178**, 1250–1260.
42 M. Hu, R. Zhao, R. Pan and G. Cao, *Int. J. Hydrogen Energy*, 2021, **46**, 18589–18603.
43 B. Kim, Y. Lee, A. Woo and Y. Kim, *Appl. Energy*, 2013, **111**, 441–448.

44 M. Matian, A. Marquis and N. Brandon, *Int. J. Hydrogen Energy*, 2011, **36**, 6051–6066.
45 T. Henriques, B. César and P. J. C. Branco, *Appl. Energy*, 2010, **87**, 1400–1409.
46 D. Qiu, L. Peng, J. Tang and X. Lai, *Energy*, 2020, **198**, 117334.
47 A. M. López-Sabirón, J. Barroso, V. Roda, J. Barranco, A. Lozano and F. Barreras, *Int. J. Hydrogen Energy*, 2012, **37**, 7289–7298.
48 J. Bhattacharya and K. Westphalen, *Semin. Immunopathol.*, 2016, **38**, 461–469.
49 M. Monjezi, M. S. Saidi and G. Ahmadi, *Sci. Iran.*, 2017, **24**, 1975–1984.
50 S. Andreassen, K. L. Steimle, M. L. Mogensen, J. Bernardino de la Serna, S. Rees and D. S. Karbing, *J. Appl. Physiol.*, 2010, **109**, 1369–1377.
51 C. B. Haeberle, A. Abreu, K. Metzler and M. Robles-Moreno, *J. Prosthodontics*, 2021, **30**, 285–289.
52 W. Pan, Z. Chen, X. Chen, F. Wang and G. Dai, *Chem. Eng. J.*, 2022, **450**, 137598.
53 J. Wang, *Appl. Energy*, 2017, **189**, 460–479.
54 F. Huang, D. Qiu, Z. Xu, L. Peng and X. Lai, *Energy*, 2021, **226**, 120427.
55 L. Fan, Z. Tu and S. H. Chan, *Int. J. Hydrogen Energy*, 2023, **48**, 7828–7865.
56 R. Stropnik, N. Mlakar, A. Lotrič, M. Sekavčnik and M. Mori, *Int. J. Hydrogen Energy*, 2022, **47**, 24223–24241.
57 D. Shi, L. Cai, C. Zhang, D. Chen, Z. Pan, Z. Kang, Y. Liu and J. Zhang, *Chem. Eng. J.*, 2023, **454**, 139995.